Structural Analysis of Potential Dual Quasar Pairs Using Galactic Modeling Software

Daniel P. Gause

Department of Physics, Middlebury College, Middlebury, VT, 05753

(Dated: December 4, 2019)

Abstract

The study of dual quasar systems has recently been of heightened interest. Quasars are actively accreting supermassive black holes embedded in the center of galaxies and are some of the most luminous objects in the universe. Quasars play an important role in galactic evolution theory, and dual quasar systems have the potential to alter their host galaxy properties. In this project, Hubble Space Telescope images of three candidate dual quasar systems were thoroughly analyzed using GALFIT, a morphological modeling program. Point Spread Functions were built using TinyTim for each source to account for optical aberrations in the Hubble Space Telescope cameras. Through GALFIT analysis, candidates were either accepted as true dual quasars or rejected as gravitational lenses, minor galaxy mergers, or other systems falsely resembling dual quasars. This study also explores whether these dual quasar candidates appeared to reside in a single shared host galaxy or distinct host galaxies. The dual quasar nature of two of these candidates was ultimately rejected, and results for the third were inconclusive.

I. INTRODUCTION

Interest in the study of quasars has been consistently growing for decades. Since their discovery in the 1960s through radio astronomy, they have quickly become some of the most studied astronomical objects. Their physical characteristics give them unique properties that allow us to peer deeper into space. They are some of the most luminous and oldest known interstellar objects. Through studying quasars, we can learn about about the large scale structure of the universe, the nature of dark matter, and the morphological evolution of galaxies. The wealth of knowledge that quasars hold is vast, and we have only begun to skim its surface.

Quasars are comprised of an accretion disk surrounding a supermassive black hole at the center of a galaxy. The mass of these black holes can range from millions to billions of times the mass of the sun. Gas, dust, and other local matter accrete around the black hole, bound by the black hole's immense gravitational force. Only a fraction of the accreted matter falls directly into the black hole, and the matter's angular momentum causes it to form a rotating disk up to several light-months across. The gravitational force from the black hole accelerates the accreting matter to extreme speeds. The viscosity between the accelerated matter in adjacent radii produces huge amounts of energy, leading to extreme luminosities ranging from 10^{45} – 10^{47} ergs s^{-1}. Quasars are excellent at converting matter into energy because the process of accretion of matter onto the black hole is energy efficient – Lambourne (2010) shows that the gravitational energy release by accretion has a theoretical efficiency of 32%. For reference, the nuclear fusion of hydrogen in stars has an energy release efficiency of only 0.7%. The immense luminosity from accreting matter is one of the unique characteristics of quasars that make their study so worthwhile, making extremely distant sources detectable due to their high absolute magnitudes.

While all quasars have accretion disks, there are a number of morphological factors that vary between individual quasars. Most quasars have a dust torus radially beyond the accretion disk. These tori can significantly obscure the light emitted from accretion disks – especially when the quasar's plane of the disk and torus are along our line-of-sight. Some quasars also have radio synchrotron radiation jets and optical jets – narrow beams of particles travelling away from the central black hole at relativistic speeds. The matter accelerated through these jets can travel up to a megaparsec, or roughly 3×10^{20} km. While the precise

cause of jets is disputed, it is generally agreed that these jets provide a feedback mechanism for quasars by injecting energy into their surroundings. In some quasar systems large radio lobes ballooning out from the central black hole are also present.

While certain components of quasars vary, their spectra are generally consistent and distinct. Inherent in quasar spectra are a number of characteristic emission lines corresponding to different regions of the quasar. There are recognizably broadened spectral lines and sharp, resolved spectral lines produced by broad line and narrow line regions respectively. There is also significant x-ray emission from the accretion disk. Quasars are tend to be old and distant objects, resulting in large redshifts of spectral lines.

Quasars give us insight into the morphological evolution of galaxies. Every quasar is hosted by a galaxy. These host galaxies are usually gas-poor ellipticals, but Courbin (2006) shows that other morphological types can host quasars. Quasars tend to be at high redshifts and their host galaxies are accordingly older and gas-poor. These galaxies are generally elliptical in morphology. Younger quasars often have gas-rich spiral or irregular host galaxies. Naab, Klochfar, & Burkert (2006) speculates on the role of early-stage galactic mergers in the origin of massive elliptical galaxies. The mechanics behind the formation of giant elliptical galaxies are not currently agreed upon, but the kinematics and luminosity patterns presented by early-stage mergers may provide a convincing explanation. The confirmation of this early-stage galactic merger theory would fill an important gap in our understanding of galaxy evolution. Commerfor & Barrows (2017) show that quasars can turn "on" or "off", transitioning between an actively accreting and dormant state. While it is not fully understood what activates quasars and fuels their feeding, Rosa, Bianchi & Bogdanovic (2016) pose theories suggesting that galaxy mergers can liberate interstellar gas from previously confined orbits, triggering star formation that could reignite dormant quasars.

Dual quasar systems are an excellent tool in uncovering the mechanisms behind these theories. Dual quasars (DQSOs) are two gravitationally bound quasars in close proximity. In order to be deemed a DQSO, the two quasars must have a separation of 10 pc to 10 kpc (systems with a separation of < 10 pc are considered binary quasars, as defined in Frey et al. (2012)). The two quasars orbit around each other and, depending on their separation and host galaxy diameters, share accreting matter. While research on DQSOs is limited, many speculate that they form when two quasar housing host galaxies merge. If this theory were to be true, DQSO systems would be an important stage in galactic development and

would give critical insight into the effect of galaxy mergers on AGN activity. Observing galaxy mergers between non-active galactic nuclei can be difficult, but, with the increased luminosity of quasars, we can pinpoint galaxy mergers at much higher redshifts, and our number of visible subjects increases. Additionally, based on the information within quasar spectra, we can make more detailed speculations into the timelines and physical conditions of specific mergers. This information would be invaluable in clarifying galactic merger and AGN activation theories.

This past summer I worked on a research project with Glikman, Ph.D. of Middlebury College and Lindsay Graham of Wellesley College searching for DQSO systems at high redshifts. There have been relatively few confirmed DQSO systems detected to date, and the theorized density of dual quasars in space suggested the existence of many undiscovered DQSO systems. We suspected that many DQSO systems had been overlooked and had been incorrectly labeled as single quasars. Ground-based telescopes cannot currently resolve sources closer than one arcsecond, so systems observed with these telescopes labeled as single quasars may be hiding multiple sources. Space telescopes mitigate atmospheric diffraction and resolve tehse sources to suitable accuracy. The Hubble Space Telescope (HST) has multiple cameras and a spatial resolution of less than 0.1 arcseconds. We built an algorithm that analyzed archival Hubble Space Telescope data containing the coordinates of known quasars. This image data was inspected, and we ultimately found 21 strong candidate dual quasar systems. Using available volume calculations, we determined that approximately 1% of the space analyzed may contain a DQSO system. If these candidates were to be confirmed as DQSO systems, our theory would be supported, proving that many DQSO systems have been overlooked. Increasing the number of known DQSOs enhances our ability to conduct research into the mechanisms behind AGN activity and long-term galaxy evolution.

II.   METHODS

Candidate Selection and PSF Generation

From our list of 21 candidate dual quasar systems, a subset was selected based on common parameters. Factors we considered included the specific Hubble Space Telescope camera used, the resolution quality, and the number of DQSO characteristics present in each can-

didate image. The list was first pared down by estimating the point source separation of each system. This was done using the redshift of each source, as the angular size is related to redshift by

$$\Delta\theta = \frac{l}{d_A} \tag{1}$$

where l is the physical size of an object and d_A is the angular diameter distance.[15] To simplify the computing process, we used Ned Wright's Cosmological Calculator (Wright (2006)), a public algorithm devoted to computing times and distances as a function of redshift for user-defined cosmological parameters. In the computation, we assumed a Hubble Constant of 69.6 $\frac{km}{s\,Mpc}$, an Ω_M value of 0.286, and an Ω_Λ value of 0.714. These parameters estimate a flat, expanding universe dominated by dark energy – the most accepted current model of the universe. The redshift of each candidate system was extracted from our compiled list of quasars and the Cosmological Calculator was used to compute the angular size. The angular size was then converted to kpc per arcsecond. The point source separation of each system was then estimated in arcseconds using DS9 software (Joye & Mandeld (2003)), by determining the two points with the greatest surface brightness, creating a line region between the two, and using the line length in arcseconds. This was then compared to the corresponding kpc per arcsecond scale to determine the separation in kpc. Candidates were classified as "promising" if the separation was under 10 kpc, and "unlikely" if the separation was greater than 10 kpc, as per our earlier stated definition of dual quasar systems. From this subset, we selected 11 candidates that exhibited the most convincing DQSO characteristics.

We then determined the HST camera used for each candidate image capture. This information was available through the MAST HST Data Search database.[21] The total number of sources from each HST camera can be found in Table I. The four HST cameras that we considered were the Wide Field Camera 3 (WFC3), the Advanced Camera for Surveys (ACS), the Wide Field and Planetary Camera 2 (WFPC2), and the Near Infrared Camera and Multi-Object Spectrometer (NICMOS). These four cameras vary in both use and age, specializing in different wavelengths and resolutions. The WFC3 and ACS cameras are the newest and most advanced, whereas the WFCP2 and NICMOS cameras are older and no longer in use. All of the HST cameras have a set of wavelength filters that allow for the imaging of specific spectra.

The varying techniques for generating point spread functions for each HST camera were then considered. Point spread functions are critical to observing and comparing astronomical

TABLE I. HST Camera Sources

HST Camera	WFC3	ACS	WFCP2	NICMOS
Counts	3	5	2	1

image data. Light incident on a camera will naturally spread due to optical lens aberrations and finite pixel size. A point spread function describes the two-dimensional distribution of a point source of light across an astronomical cameras focal plane. PSFs vary widely between cameras, as each camera has a different lens and pixel data processing method. Additionally, the PSF of a single camera can vary depending on the position of the target source on the lens itself. As quasars and stars are point sources of light, generating accurate PSFs was crucial to this project. Thus, the PSF generating techniques for each HST camera were considered in choosing which candidate systems to analyze.

In general, PSFs are generated empirically by sampling a subset of stars surrounding the target position in an image. By averaging the spread of light from each of these point sources, one can build a function that adequately describes the point spread of a position on a specific camera lens. While this method is reliable, it can be both tedious and time intensive. Thus, it is preferable to use existing algorithms for generating PSFs analytically. One such algorithm is TinyTim (Krist & Hook (2011)), a software package developed by the Space Telescope Science Institute (STScI) for generating HST PSFs. TinyTim is written and distributed in C, and runs on UNIX systems. It requires the input of a FITS astronomical image file, the HST camera and detector number, the position on the focal plane of the detector, the filters used in image capture, the form of the target object's spectra, and the required PSF size. TinyTim then uses these parameters along with the specific diffraction patterns of the chosen camera to estimate a PSF through a sum of Zernike polynomials – a set of polynomials orthogonal on the unit disk. Zernike polynomials are much like spherical harmonics but are applied to two-dimensional systems.

TinyTim has PSF generating capabilities for all of the HST cameras, but with varying levels of effectiveness. It is generally accepted that PSFs generated for the ACS and WFCP2 cameras by TinyTim are the most accurate, while the PSFs generated for the WFC3 and NICMOS cameras are of lower quality. For this reason, along with the high number of DQSO candidates with ACS image data, we decided to focus our modeling efforts on the

ACS candidates. The generated ACS PSFs were customized by using a custom quasar spectrum, sourced from Telfer et al. (2002) combined with Vanden Berk et al. (2001). It is necessary to use a custom spectrum, as there is a wavelength dependence for the PSF. Light at various wavelengths will interact and diffract with the camera apertures differently, resulting in a different PSF. By using a quasar spectrum, we accounted for these differences. A visualization of the quasar spectrum we used from 0 Å to 10000 Å can be found in Fig 1.
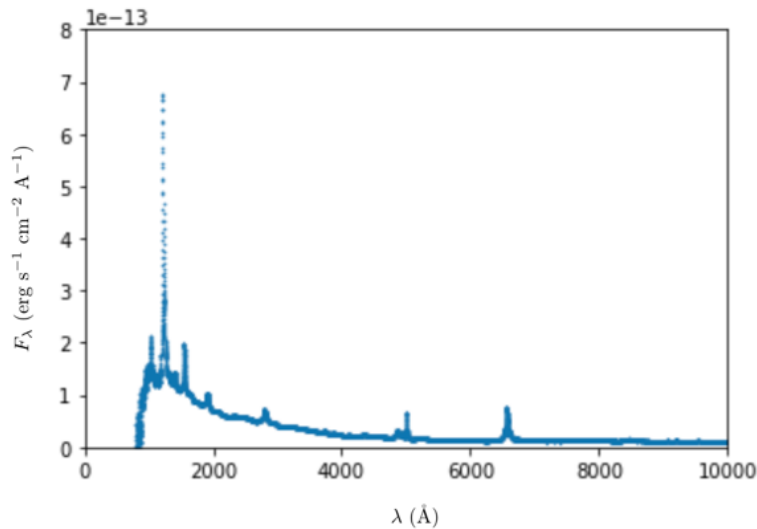

FIG. 1. Quasar spectrum used for TinyTim PSF generation. (wavelength (Å) vs flux (erg/s/cm2/A))

Multicomponent Fitting with GALFIT

After generating the PSFs for our ACS imaged DQSO candidates, we began the process of modeling. Our method used the morphological fitting program, GALFIT, which was first introduced in Peng et al (2002). GALFIT is a widely used open source software package used to extract information about interstellar objects by using parametric functions to model objects as they appear in two-dimensional digital images. GALFIT takes an image file of an object, a corresponding PSF, and a set of image and function component parameters and generates a surface brightness model. See Figures 2 and 3 for examples of GALFIT input files. The surface brightness profiles of various astrophysical objects can be simulated

7

through a set of analytic functions available in GALFIT. Objects such as stars and quasars have point source surface brightness profiles, whereas elliptical and spiral galaxies follow more complex profiles.

```
========================================================================
# IMAGE and GALFIT CONTROL PARAMETERS
A) j8pu0b010_drz.fits[SCI]    # Input data image (FITS file)
B) 10_24output.fits         # Output data image block
C) none                # Sigma image name (made from data if blank or "none")
D) spectra_PSF00.fits         # Input PSF image and (optional) diffusion kernel
E) 1                   # PSF fine sampling factor relative to data
F) none                # Bad pixel mask (FITS image or ASCII coord list)
G) none                # File with parameter constraints (ASCII file)
H) 2120   2190   1490  1560  # Image region to fit (xmin xmax ymin ymax)
I) 100    100          # Size of the convolution box (x y)
J) 26              # Magnitude photometric zeropoint
K) .005  .005        # Plate scale (dx dy)   [arcsec per pixel]
O) regular             # Display type (regular, curses, both)
P) 0                   # Choose: 0=optimize, 1=model, 2=imgblock, 3=subcomps
```

FIG. 2. An example of GALFIT image input parameters in UNIX.

```
# Object number: 4
0) sersic
1) 2155 1530  1 1  #  position x, y
3) 20     1     #integrated magnitude
4) 5.5      1 #R_e (half-light radius) [pix]
5) 5      1      #sersic index n( de vaucoleurs n=4)
9) 0.6      1   #axis ratio (b/a)
10) 10 1                 #position angle (PA) [deg: up=0, left=90]
F1) 0.0001 0.0000 11    #azim. fourier mode 1, amplitude, & phase angle
F3) 0.0001 0.0000 11    #azim. fourier mode 3, amplitude, & phase angle
Z) 0
```

FIG. 3. An example of a GALFIT function component input in UNIX.

With an image file, a PSF, and various other parameters as inputs GALFIT uses a Levenberg-Marquardt algorithm to minimize the residual between the original image and the mathematical model. The Levenberg-Marquardt algorithim, described in Ranganathan (2004) and also known as the damped-least squares method (DLS), is a solution to the nonlinear least squares problem. This statistical method is an iterative procedure that aims to minimize the reduced chi-squared value, χ_ν^2. χ_ν^2 is defined in the standard way as

$$\chi_\nu^2 = \frac{1}{N_{\text{dof}}} \sum_{x=1}^{nx} \sum_{y=1}^{ny} \frac{(\text{flux}_{x,y} - \text{model}_{x,y})^2}{\sigma_{x,y}^2} \tag{2}$$

where

$$model_{x,y} = \sum_{\nu=1}^{nf} f_{\nu,x,y}(\alpha_1...\alpha_n) \ . \tag{3}$$

N_{dof} is the number of degrees of freedom in the fit, nx and ny are the x and y image dimensions, and flux$_{x,y}$ is the sum of the nf functions $f_{\nu,x,y}(\alpha_1...\alpha_n)$ employed, where $\alpha_1, ..., \alpha_n$ are the two-dimensional model parameters. The non-reduced chi-squared value is simply the reduced chi-squared value multiplied by the degrees of freedom. GALFIT adjusts the

function component parameters in small increments, iterating through models to find the model that minimizes χ^2_ν of the pixel intensity. The collection of components and parameters that minimizes χ^2_ν in GALFIT most accurately models the surface brightness profile of the input image.

The image data *fits* files for each candidate DQSO source were downloaded from the STScI MAST Portal. This online database allows images to be retrieved based on each target's position coordinates on the sky. All available calibrated files containing that coordinate position were then batch downloaded, filtering out any uncalibrated data files. STScI uses an image calibration program known as AstroDrizzle (Fruchter & Hook (2002)). Drizzling is a form of astrometric image reduction commonly applied to Hubble data that stacks multiple *fits* files of the same image in order to remove stray cosmic rays and to reduce background noise and pixelation errors. We then piped the relevant *fits* data image files into a python script that cropped the image to a 100×100 pixel cutout of our candidate DQSO system. This cutout was the image file we used to create our PSFs and for GALFIT fitting.

A variety of component combinations were then tested on each candidate DQSO source to determine which model best fit the system, and the component parameters and χ^2 statistical values were recorded. Every candidate featured two distinct luminosity sources of varying apparent magnitudes and separations. General observational information on each source can be found in Table II. A DQSO system would most likely exhibit two quasar components with PSF surface brightness profiles each embedded in a host galaxy component. It is possible for two quasars to be embedded in a single host galaxy, but the resolution necessary to observe these small scale separations can be hard to attain in HST ACS images. For our sources, Sérsic functions were used to model host galaxy radial surface brightness profiles. These profiles, developed in Sérsic (1968), are given by the equation

$$\Sigma(r) = \Sigma_e \exp \left[-\kappa \left(\left(\frac{r}{r_e} \right)^{1/n} - 1 \right) \right] \qquad (4)$$

where r_e is the effective radius within which half the total flux is contained, Σ_e is the surface brightness at the effective radius, and n is the Sérsic index. The value of the Sérsic index changes the modeled galaxy morphology: $n = 4$ generally represents elliptical galaxies, $n = 1$ represents spiral galaxies, and $n = 0.5$ is a two-dimensional Gaussian distribution.

A single PSF was initially fitted to each luminosity peak, representing two point sources

TABLE II. Candidate DQSO Systems imaged with *HST* ACS

Source Name	RA.	Dec.	Redshift	Filters	Exposure Time (s)	Zero Point Mag	Separation (kpc)
4C24.10	5:16:03.20	+24:58:25.00	0.063	FR716N	400	-21.1	0.611
				FR647N	60	-21.1	
				FR551N	500	-21.1	
COSMJ10020+0201	10:02:03.74	+2:01:45.01	0.898	F814W	2028	-21.1	2.09
PSS J2322+1994	23:22:07.13	+19:44:22.99	4.17	F814W	2028	-21.5	10.461

without host galaxies. This model was used as an initial benchmark to which we compare more complex models. A Sérsic component was then layered behind one of the PSFs, leaving one PSF standing alone. This model resembled a system with a single quasar embedded in a host galaxy and a less distant line-of-sight star. The Sérsic component was then to the other PSF. The stand alone PSF was then replaced with a Sérsic component, modeling a system with an active AGN and a nearby galaxy with an inactive galactic nucleus. The PSF was then switched to the other Sérsic component. The second PSF was then added back, embedding each PSF in a host galaxy Sérsic radial profile. This model represented the dual quasar system the study was testing for. If the source exhibited additional features, such as tidal arms or nearby extraneous luminosity sources, we adjusted our model components as we saw fit. Finally, to check for overfitting, an additional host galaxy Sérsic component was added to our model and we observed how it affected the χ^2_ν value. This process is illustrated in a schematic in Fig 4.

The χ^2_ν values were compared for each consecutive fit, and an F-test was used to determine the improvement between modeling stages. An F-test gives the probability for a particular reduction in total χ^2 relative to change in number of degrees of freedom (DOF). To calculate the F value between successive fits, we used the formula

$$F = \frac{(\chi_1^2 - \chi_2^2)/(DOF_1 - DOF_2)}{(\chi_2^2/DOF_2)} \tag{5}$$

where χ_1^2 and χ_2^2 are the non-reduced chi-squared values of the successive fits and DOF_1 and DOF_2 are the degrees of freedom for each model. Using this F value, we then used the function **MPFTEST** in IDL to compute the probability in standard deviations for a value
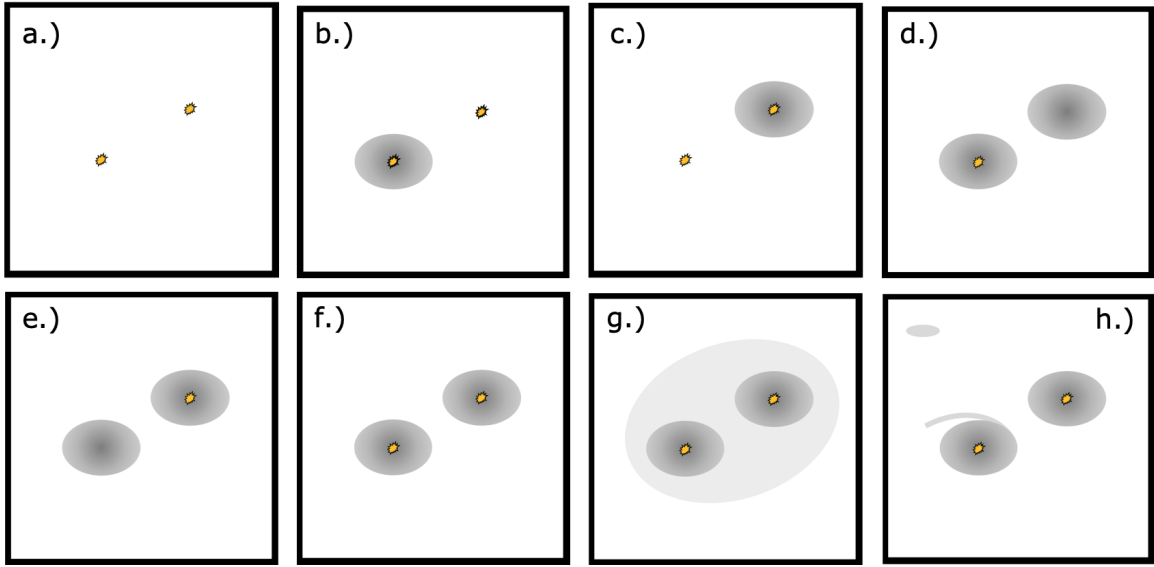
FIG. 4. The GALFIT component modeling method. Each consecutive frame represents an additional modeling stage. The points represent PSF components, while the larger ellipses represent Sérsic components. The large ellipse in g.) represents an additional Sérsic component to test for overfitting. The smaller ellipse and non-symmetric arm in h.) represent any additional features we attempted to fit.

drawn from the F-distribution to equal or exceed the given value of F.[9] Fit was significantly improved if it returned a value $> 10\sigma$ in the F-test. Any fits returning values $< 10\sigma$ were suspected of overfitting.

III. RESULTS

We preformed the multiple stages of GALFIT analysis on three different candidates – 4C24.10, COSM J10020, and PSS J2322. Their separate PSFs built using TinyTim can be found in Fig. 5. We decided to focus on different modeling stages for each candidate based on the general nature of each source. The results of these fits can be found in Table III. The remainder of this section will focus on each individual candidate.

TABLE III. Candidate DQSO Systems imaged with *HST* ACS

| Source Name	Model Stage	Y_{PSF1} (mag)	Y_{PSF2} (mag)	Y_{SER1} (mag)	Y_{SER2} (mag)	R_{SER1} (pixels)	R_{SER2} (pixels)	n_{SER1}	n_{SER2}	χ^2	ν (N_{DOF})	χ^2_ν
4C24.10 (FR716N)	(a)	18.16	18.09	...	...	...	...	...	...	7447.22	10194	0.731
comp	(b)	18.29	18.28	14.61	...	83.66	...	2.04	...	6432.29	10185	0.632
comp	(h1)	18.16	18.10	...	...	...	...	...	...			
secondary PSFs		20.04	20.50	...	...	...	...	...	...	7365.356	10188	0.723
comp	(h2)	19.86	20.37	17.04	16.90	3.70	3.70	5.05	4.45			
secondary PSFs		20.03	20.56	...	...	...	...	...	...	6689.47	10172	0.658
comp	(h3)	18.99	19.33	16.97	16.55	[10]	[10]	6.15	4.637			
secondary Sérsics				17.93	18.52	[8.15]	[5.96]	2.37	0.65	6313.77	10162	0.621
COSM J10020	(a)	22.43	22.77	...	...	...	...	...	...	3882.99	5034	0.721
comp	(b)	22.99	23.382	21.31	...	5.64	...	0.974	...	3033.40	5027	0.603
comp	(c)	22.98	23.30	...	24.31	...	5.22	...	0.95	2702.28	5025	0.538
comp	(d)	28.83	...	21.0	22.01	2.99	2.46	3.19	2.78	2679.13	5019	0.534
comp	(e)	...	22.96	21.88	21.83	4.75	2.74	1.11	3.25	2623.08	5019	0.523
comp	(f)	23.00	23.84	21.78	22.15	4.71	3.30	1.14	2.57	2612.77	5016	0.521
PSS J2322	(a)	20.73	18.66	...	...	...	...	...	...	7532.8	10914	0.739
comp	(b)	18.89	20.73	20.04	...	0.17	...	10.81	...	7011.58	10185	0.688
comp	(c)	18.65	21.42	...	20.50	...	0.155	...	19.99*	9040.19	10185	0.888
comp	(d)	18.66	...	21.18	21.29	1.29	0.18	4.2	0.58	7302.13	10179	0.717
comp	(e)	...	21.42	18.57	21.32	0.01	0.70	4.54	0.04	26830.12	6179	2.636
comp	(f)	18.66	21.22	19.67	21.24	0.01	1.01	15.69	10.09	7161.34	10176	0.704
comp	(h1)	18.66	20.75 (25.44)**	22.07		16.02		[4.0]		6750.04	10183	0.663
comp	(h2)	18.82	(20.74)	20.26.31	22.23	0.48	10.19	[4]	[4]	6489.90	10178	0.638
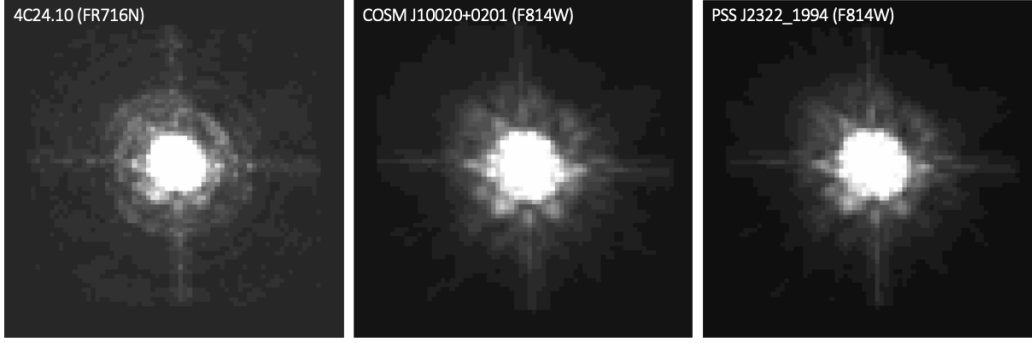
FIG. 5. PSFs used in modeling for three DQSO candidate sources generated through TinyTim. They are shown using a logarithmic scale to highlight unique characteristics.

4C24.10

Overall fit

For 4C24.10, we skipped modeling stages (c) through (g) as this source had two clear secondary sources that significantly affected intermediate models. After modeling stages (a) and (b), we included additional components to account for the two secondary sources. We initially modeled the secondary sources as PSFs, which only slightly improved the fit, reducing the χ_ν^2 value from 0.731 to 0.723. These consecutive fits returned a F-test value of 33.16σ. Adding additional Sérsic components behind the primary point sources while retaining the secondary PSFs reduced χ_ν^2 to 0.658. Finally, by exchanging the secondary point source PSFs for Sérsic components, we obtained a fit with a χ_ν^2 value of 0.621. Comparing this to our next best fit in model stage (b), an F-test returned 23.72σ. As this was greater than our significant value of 10σ, we accepted (h3) as our best fit. Embedding additional PSFs in the secondary point source Sérsic components had no effect on the χ_ν^2 value. During this particular fitting process, we found that Sérsic components tended to explode, resulting in unreasonably high magnitudes and effective radii, as is evident from the Sérsic component in model stage (b). Thus, we held the effective radii parameter of our Sérsic components fixed. This affected the overall fit, but kept our parameters reasonable. We attributed this effect to GALFIT's tendency to stretch Sérsic components to blanket images with high background noise. Our final fit can be viewed in Fig 6.

12

Systems and host galaxy morphology

This fit represents two quasars, each embedded in separate host galaxies, with two unaffiliated nearby galaxies. While this astrophysical structure is possible, we find gravitational lensing to be a much more likely explanation. This asymmetric quadruple lensing pattern is common among quasars as shown by Myers and Fassnacht (1995). With no visible lensing object, the lensing mass is expected to be a galaxy at too high a redshift to be visible. In the case of a gravitational lens, we would be observing the light from a single quasar distorted by the lensing mass into four sources. These sources would have the same spectra and surface brightness profiles, but would vary in intensity. Thus, we would expect four PSFs all embedded in separate host galaxies. Our most accurate fit agrees with this model, except neither proves nor disproves the presence of PSFs embedded in the secondary Sérsic components. This loss of information may be due to the high background noise of the image and relatively low surface brightness of the secondary sources.
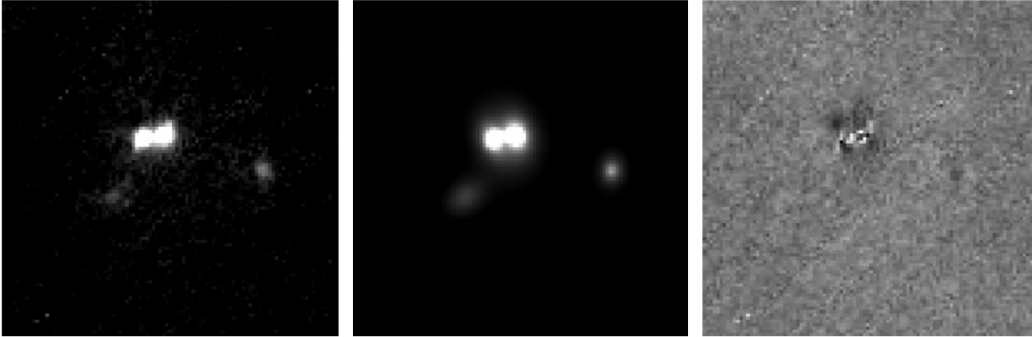
FIG. 6. The 4C24.10 source through the FR716N filter, the GALFIT produced model using fit stage (h3), and the corresponding residual.

COSM J10020

Overall fit

For COSM J10020, we decided to complete stages (a) through (g) given in Fig 4. This source had few background artifacts in the 100×100 pixel cutout, allowing us to skip stage (h). Our PSF only fit produced a χ^2_ν value of 0.721. This reduced chi-squared value was significantly larger than that of any following fits but gave us a sense of appropriate magnitudes

to assign each peak. The two magnitudes were 22.43 and 22.77 respectively, suggesting that the two sources contributed similar luminosities to the overall surface brightness profile. In the following 5 modeling stages, we saw gradual improvement in χ^2_ν values. By layering a single Sérsic component behind one of the PSFs, we reduced the χ^2_ν to 0.608, returning 201.14σ from an F-test. The model and residual images for fit (b) can be found in Fig. 7. Every time we added a Sérsic component, we held its position parameters constant. Otherwise the Sérsic component tended to drift towards the center of the system and spread to account for more luminosity. By holding the position parameters constant, we retained the effect of modeling two individual galaxies. An F-test for the χ^2_ν values between our model stages (d) and (e) returned a value of 10.30σ – which approached the significance cutoff of 10σ. Our final fit, (f), had the lowest χ^2_ν value of 0.521. This fit included two PSFs, each embedded in a host galaxy. While fit (f) had the lowest χ^2_ν value, an F-test comparing it to fit (e) returned a value of 3.73σ, below our established cutoff. The model and residual images for fit (f) can be found in Fig. 8.

The magnitudes of both model host galaxy's Sérsic components were significantly higher than their corresponding PSFs. This behavior is unexpected in dual quasars, as the host galaxies are normally several orders of magnitude less luminous. As all magnitudes are integrated over the entire component, the relative spread of the Sérsic components compared to PSFs may account for the higher magnitudes. We attribute some modeling imperfections to fixing Sérsic parameters in order to prevent spreading in accounting for background noise, but cannot fully rely on fit (f) as the best fit.
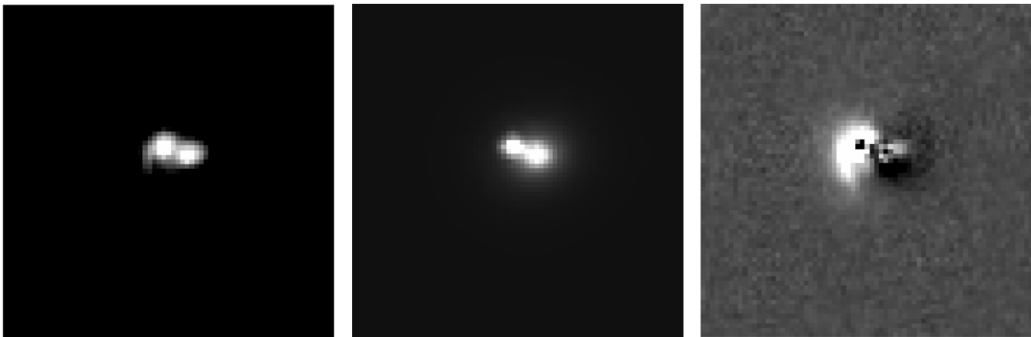

FIG. 7. The COSM J10020 source, the GALFIT produced model using fit stage (b), and the corresponding residual.
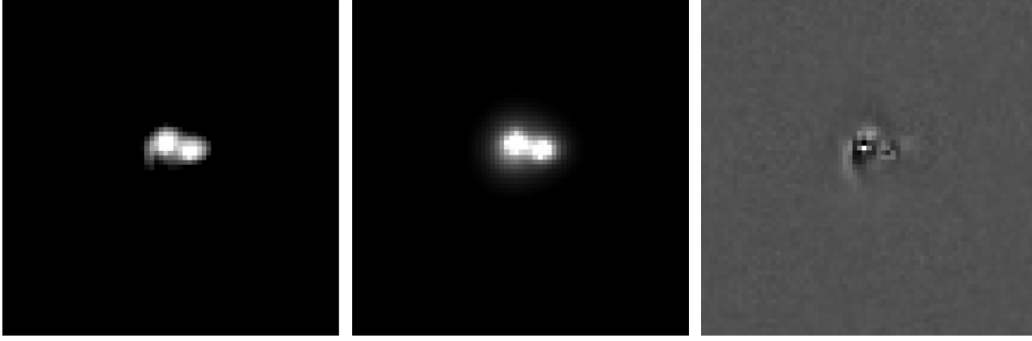
FIG. 8. The COSM J10020 source, the GALFIT produced model using fit stage (f), and the corresponding residual

Host Galaxy Morphology

If we were to assume the model of fit (f) was correct, there were two separate host galaxies, both following Sérsic surface brightness profiles. The first host galaxy had a Sérsic index of 1.14, and the second had an index of 2.57. These Sérsic indices generally correspond to spiral and elliptical morphologies respectively. To visualize these morphologies, we first subtracted the PSFs from the original source cutout, then we separately plotted the two Sérsic models produced in GALFIT, which can be viewed in Fig. 9.

In the leftmost host galaxy, there is an obvious arm protruding from the galactic edge. While this could suggest a spiral morphology, there is no visible counterpart spiral arm on the opposite galactic edge. A suitable alternative explanation behind this protruding arm is the existence of a tidal tail. Tidal tails, as explained in Freedman (2014), are elongated regions of stars and interstellar gas that form due to galactic tide forces in galactic interactions. The presence of a tidal arm would suggest a past or concurrent galaxy merger, which constitutes direct evidence of dual quasar characteristics. It would also explain any deficiencies in our Sérsic model – GALFIT has limits in modeling asymmetric models, and modeling exterior arms lies outside the scope of this project. This potential tidal tail paired with our convincing DQSO GALFIT model make source COSM J10020 a highly probable DQSO candidate.
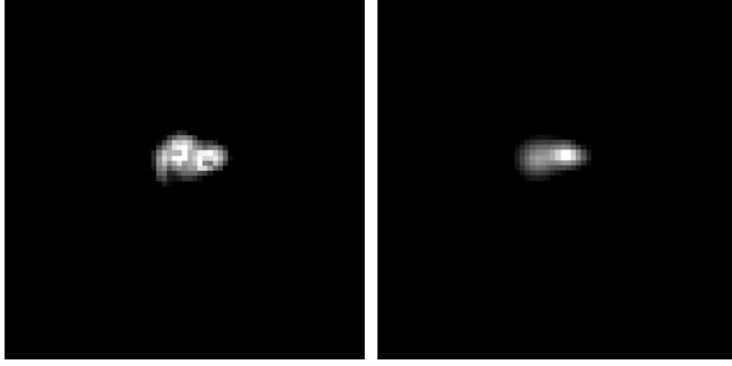
FIG. 9. The COSM J10020 source with PSFs subtracted, and the GALFIT model of the two host galaxies with Sérsic profiles

PSS J2322+1994

Overall fit

For source PSS J2322+1994 we decided to complete modeling stages (a) through (h). Our initial fit with two PSFs returned a χ^2_ν value of 0.739. In testing subsequent models, we found that while adding a Sérsic component to the lower source improved the fit, embedding the upper PSF in a Sérsic component significantly degraded the quality of the fit. By adding a Sérsic to the upper source in stage (c), the χ^2_ν value rose to 0.888. Removing the PSF for the lower source in stage (e) resulted in a χ^2_ν value of 2.636. In our (h) stages, by including an additional PSF to account for the dimmer, secondary source between the two main sources, the χ^2_ν value improved to 0.663. In comparing this fit to our second best fit, (h), and F-test resulted in a value of 23.86. In our final fit, we removed the upper PSF, and replaced it with a Sérsic component, greatly improving our fit. This final fit, which can be viewed in Fig. (10), had a χ^2_ν value of 0.638. Comparing this fit to (h1) through an F-test resulted in a value of $> 35\sigma$, so we can definitively say that fit (f) was the best.

Systems and host galaxy morphology

Our final model for PSS J2322+1994 represents a single quasar embedded in a host galaxy, a nearby star, and a nearby galaxy. This system does not directly resemble a dual quasar. While it exhibits some visual lensing attributes, a gravitational lens would include an
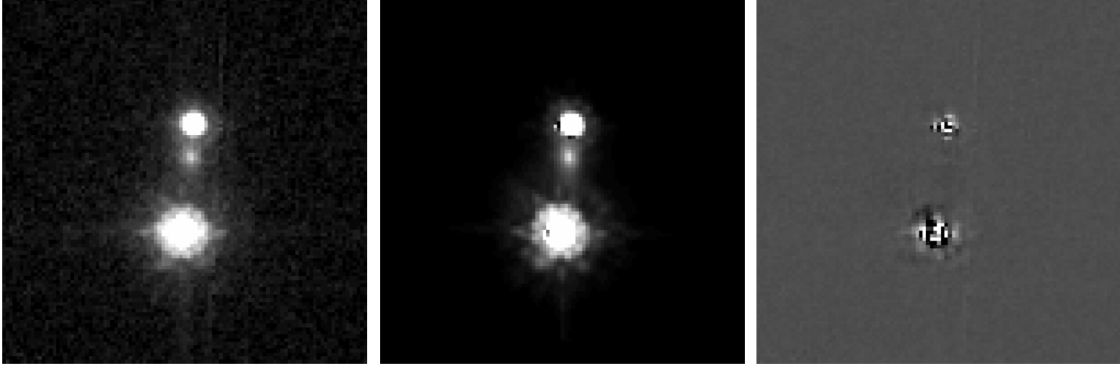
16

FIG. 10. The PSS J2322+1994 source, the GALFIT produced model using fit stage (h), and the corresponding residual

embedded PSF component in both sources. The fit aversion to a PSF component embedded in the upper source therefore contradicts the gravitational lens explanation. There was significant noise in this image, and GALFIT tended to smear the Sérsic components to compensate for the background. For this reason, we kept a number of the Sérsic parameters fixed, limiting the precision of the fit. We held both Sérsic components in fit (f) at the de Vaucouleurs profile Sérsic index, $n = 4$.

IV. CONCLUSION

Dual quasar systems play an important role in galactic evolutionary theory. They allow us to observe galaxy mergers that would otherwise be too distant to detect. The gravitational and morphological interactions between quasars and their host galaxies in dual systems sheds light on contested theories of how giant ellipticals form and why AGN can activate and deactivate. Our list of known dual quasars is short, thereby limiting the knowledge we can draw from these systems. For this reason, detecting new dual quasar systems and studying their host galaxy morphologies is necessary.

In this project we hoped to achieve this by examining three dual quasar candidates in detail. We built point spread functions using TinyTim for each candidate based on cosmological parameters and camera settings. We developed a surface brightness modeling method to determine the morphology of each system, which we executed through the mathematical modeling software GALFIT. Our modeling method aimed to reveal the interstellar objects

present in each system, whether they may be quasars embedded in host galaxies, unaffiliated line-of-sight stars, or merging galaxies. Through GALFIT we visually observed models and residuals, and computed reduced chi-squared values for each fit which we compared through F-tests. Two out of the three candidates had definite best-fit models, while one candidate had unclear results. The best model for source 4C24.10 suggested a single quasar quadruply gravitationally lensed by a line-of-sight mass. Our models for the COSM J10020 source were less clear – while the dual quasar model returned the lowest χ_ν^2 value, it was only 3.73σ away from the next best fit in an F-test, below our cutoff of 10σ. For this reason, we could not definitively confirm this source as a dual quasar. Despite this uncertainty, we detected what appeared to be a tidal arm in one of the Sérsic components of the system, evidencing a recent galactic merger. Our model for source PSS J2322 was more conclusive, as our best fit did not agree with a dual quasar system. More likely, this source was either the gravitational lens of a single quasar, or a single quasar with an unaffiliated galaxy and star nearby.

In summary, we can confidently reject the sources 4C24.10 and PSS J2322 as dual quasar systems. While our model for COSM J10020 was inconclusive, this source exhibited multiple characteristics seen in dual quasars and galaxy mergers. Further research including analysis with multiple spectral filters and higher resolution images would quickly reveal the underlying morphology of this system.

---

[1] Comerford, J. M., Barrows, R. S, et al. 2017, *An Active Galactic Nucleus Caught in the Act of Turning Off and On.* ApJ, 849, 2

[2] Courbin, F., Letawé, G., et al. 2006, *The Host Galaxies of the Brightest Quasars: Gas-Rich*

Galaxies, Mergers, and Young Stars. The Messenger, 124, 32

[3] Rosa, A., Bianchi, S., Bogdanovic, T., et al. 2016, *Unveiling multiple AGN activity in galaxy mergers.* Astronomische Nachrichten, 338, 10

[4] Joye, W. A., Mandel, E., 2003, *New Features of SAOImage DS9.* Astronomical Data Analysis Software and Systems, 295, 489

[5] Freedman, R. A. (2014) *Universe.* New York, NY: W.H. Freeman and Company

[6] Frey, S., et al. 2012, Two in One? *A Possible Dual Radio-Emitting Nucleus in the Quasar SDSS J1425+3231.* Monthly Notices of the Royal Astronomical Society 425.2 1185

[7] Fruchter, A. S., & Hook, R. N. *Drizzle: A Method for the Linear Reconstruction of Underampled Images.* Publications of the Astronomical Society of the Pacific, 2002.

[8] Lambourne, Robert J. A. 2010. *Relativity, Gravitation and Cosmology* (Illustrated ed.). Cambridge University Press. p. 222.

[9] Research Systems, Inc. 1995. IDL user's guide : interactive data language version 4. Boulder, CO :Research Systems,

[10] Myers, S. T., Fassnacht, C. D., et al. 1995, *1608+656: A Quadruple-Lens System Found in the CLASS Gravitational Lens Survey.* ApJ, 447, 1

[11] Naab, T., Khochfar, S., Burkert, A., 2006, *Properties of Early-Type, Dry Galaxy Mergers and the Origin of Massive Elliptical Galaxies.* ApJ, 636, 2

[12] Wright, N., 2006, *A Cosmology Calculator for the World Wide Web.* PASP, 118, 1711.

[13] Peng, C. Y., Ho, L. C., Impey, C. D., & Rix, H. W. 2002, *Detailed Structural Decomposition of Galaxy Images.* AJ, 124, 266

[14] Ranganathan, A. 2004, *The Levenberg-Marquardt algorithm*

[15] Ryden, B. 2003, *Introduction to Cosmology.* San Francisco, CA: Addison Wesley

[16] Sérsic, J. L. 1968, Atlas de galaxias australes (Cordoba: Observatorio Astronomico)

[17] Taylor, M. B. 2005, in ASP Conf. Ser. 347, Astronomical Data Analysis Software and Systems XIV, ed. P. Shopbell, M. Britton, & R. Ebert (San Francisco, CA: ASP), 29

[18] Telfer, R., Zheng, W., et al. 2002, *The Rest-frame extreme ultraviolet spectral properties of QSOS* AJ. 565 773

[19] Krist, J. E., Hook, R. N., & Stoehr, F. 2011 *20 years of Hubble Space Telescope optical modeling using Tiny Tim.* Proceedings of the SPIE, Volume 8127

[20] Vanden Berk D. E., et al., 2001, *Composite Quasar Spectra from the Sloan Digital Sky Survey.*

AJ, 122, 549

^{21} Https://archive.stsci.edu/hst/search.php